Structural Analysis and Thermal Behavior of Pore Networks in High-Surface-Area Metal−Organic Framework

Cheng-Si Tsao,*,†,∥ Chun-Yu Chen,‡ Tsui-Yun Chung,† Chun-Jen Su,§ Chiu-Hun Su,§ Hsin-Lung Chen,‡ U-Ser Jeng,§ Ming-Sheng Yu,† Pin-Yen Liao,† Kin-Fu Lin,† and Yi-Ren Tzeng†

Institute of Nuclear Energy Research, Longtan 32546, Taiwan, Department of Chemical Engineering, National Tsinghua University, Hsinchu 30076, Taiwan, National Synchrotron Radiation Research Center, Hsinchu 30076, Taiwan, and Departemt of Nuclear Science and Engineering, Massachusetts Institute of Technology, Cambridge, Massachusetts 02139

Received: July 26, 2009; Revised Manuscript Received: March 6, 2010

Metal−organic framework-5 (MOF-5) with high surface area was synthesized in this study. The complete picture of pore structure in the crystal from the locally perfect micropore channels to the global mesopore network distributed along the constituent micrograins was revealed by small-angle X-ray scattering (SAXS). The in situ SAXS measurement was conducted to investigate the concurrent evolution of mesopore structure and micrograin boundary during heating and thermal activation at 200 °C. During the pore evacuation and formation of micrograin boundary, the flexible mesopores shrink, swell, and realign, while the micropores remain stably rigid. The result shows the role of the tunable mesopore network in the MOF-5 crystal governing the migration of gas molecules. This new finding will be useful for guiding the rational crystal design and the synthetic modification for improving the crystal quality in potential applications.

Introduction

Crystalline metal−organic framework (MOF)[1−6] has attracted considerable attention for a wide range of applications, including hydrogen storage, chemical separation,[7] and catalysis,[8] because of its very high specific surface area (SSA; >3000 m^2/g) and microporosity. The ordered framework comprised of metal−carboxylate coordination moieties and tunable organic linkers has an open 3D pore network, which effectively enables gas diffusion into its interior space. The high SSA is attributed to the 3D channel structure[2] formed by ordered and mutually orthogonal 1D pore channels. The intersection space of orthogonal pore channels can be regarded as spherical pore with aperture (pore diameter < 2 nm). In fact, the BET SSA values of the most well-known MOF-5 crystals synthesized by different laboratories[9−11] vary widely and are usually less than 1500 m^2/g. By examination of X-ray diffraction (XRD) patterns, these crystals[11] were found to have (1) metal cluster or residual defects in the nanocavity and (2) unwanted lattice interpenetration, which result from the collapsed framework during the crystal formation. These lattice defects significantly block the diffusion of nitrogen gas in the pore channel and thus reduce the measured SSA value.[12,13] The synthesis of high-surface-area MOF-5 crystal (as an example) remains a challenging task because of the difficulties[14−16] in the preparation. A substantial variation of Langmuir SSA values of MOF-5 crystals from 3362[3] and 4170[4] to 4400[14] m^2/g was recently reported by Yaghi's group. Moreover, the experimental characterization of the pore structure in MOF is very limited to date, although the porous nature of real MOF crystals including the open characteristic is a key in determining the hydrogen storage capacity via physisorption.

The gas sorption analysis generally adopted for characterizing pore structure has several limitations,[17] which include (1) diffusional hindrance of gas, (2) closed porosity,[18] (3) different interactions between gas and adsorbent, and (4) different models/assumptions adopted for micropore (assuming slit-like geometry) or mesopore (assuming cylindrical geometry). Therefore, the results of pore analysis obtained from different models in gas adsorption differ significantly from one another. By contrast, small-angle X-ray scattering (SAXS) can accurately resolve the size, geometry, and network of the pores at different length scales as well as their spatial arrangements, demonstrating the advantages over the usual techniques.[17−20] Apparently, SAXS characterization will be able to gain significant insight into the real pore structure.

The reduction in SSA value of MOF has also been attributed to channel collapse upon solvent removal or channel blockage due to the residual solvent.[21] Two treatments usually adopted to remove the solvent contained in MOF are (1) thermally assisted evacuation of the solvent (i.e., conventional activation) and (2) liquid solvent exchange followed by a degas process or pore evacuation at moderate temperature. Recently, a new route for effectively enhancing the SSA value of MOF materials was reported by Hupp's group.[22] They considered the special activation preventing the mesopore collapse as the main key and hypothesized that thermal evacuation of solvent causes the collapse of interparticle mesopores and the misalignment of micropores at particle/particle boundaries inhibits access by gas molecules to internal (microporous) surfaces. Our previous study[23] also consistently supported that the mesopores between the micrograins is the main path of the gas molecules migrating into the local micropores from the outer surface followed by adsorbing to the internal surface sites. Mesopore also plays a possible role to affect the SSA value and other properties, but

* To whom correspondence should be addressed. E-mail: cstsao@iner.gov.tw.
† Institute of Nuclear Energy Research.
∥ Massachusetts Institute of Technology.
‡ National Tsinghua University.
§ National Synchrotron Radiation Research Center.

10.1021/jp907103r © 2010 American Chemical Society
Published on Web 03/30/2010

its associated mechanism is not clear. Moreover, the structures of the mesopore and the micrograins and their spatial correlation and orientation were rarely investigated and have indeed never been directly evidenced.

In this study, we synthesized a MOF-5 with Langmuir SSA value of ~4700 m^2/g and the XRD pattern consistent with the theoretically calculated one. Detailed SAXS characterization of this high-SSA MOF-5 almost without lattice defects was then conducted to identify the pore channel and the formed 3D network for the first time. A plausible structure model was adopted to analyze the SAXS profiles quantitatively, from which the size, geometry, and spatial network associated with different pore structures were revealed on the micropore scale (≤2 nm) to the mesopore scale (between 2 and 50 nm). To accurately resolve the local MOF structure with the length scale less than 2 nm, the anomalous synchrotron SAXS experiment was performed to investigate the significant effect of the electronic structure of the microporosity. The present investigation of pore structure for such a high-SSA MOF reveals how the crystal structure evolves from the locally perfect micropore channel toward the global mesopore network distributed along the constituent micrograins. This new finding will be useful for guiding further synthetic modification for potential applications of gas adsorption via pore-controlling approach.

The present study also performed an in situ SAXS measurement to investigate the concurrent evolution of mesopore structure and micrograin boundary during heating and subsequent thermal activation at 200 °C. The temperature- and time-dependent SAXS profiles corresponding to these steps revealed the mutual relation between mesopore and micrograin, and their thermal behavior. It will be shown that during the pore evacuation and formation of micrograin boundary, the flexible mesopores shrink, swell, and realign, while the micropores remain stably rigid. This experimental result not only verified the previous hypotheses but also provided useful knowledge for further understanding the storage and migration of gas molecules in the MOF-5 crystal governed by the tunable mesopores.

Experimental Methods

Sample Preparation. A 1.56 g sample of zinc nitrate tetrahydrate ($Zn(NO_3)_2 \cdot 4H_2O$, Merck) and 0.33 g of terephthalic acid (BDC, Fluka) were added into 50 cm^3 of *N*,*N*-diethylformamide (DEF, TCI) solvent in a 250 cm^3 glass capped with rubber. The solution preparation was carried out in a glovebox. After sufficient stirring, the DEF solution was equilibrated at 120 °C for 12 h, and then cooled to room temperature at a cooling rate of ~1.6 deg/min[23] followed by transferring to a nitrogen-filled glovebox. The solid product was filtered off and then washed in DEF three times followed by several times of $CHCl_3$ solvent exchange. All procedures were controlled under minimization of exposure to water and air.[14] The obtained MOF-5 crystals of cubic shape were denoted as MOF-5_A. Some MOF-5_A crystals were subsequently thermally activated at 200 °C for 3 h under vacuum for removing the residual chloroform and other guest molecules. The resulting material was denoted as MOF-5_B. The powder XRD pattern measured with a Bruker D8 (operated at 40 kV and 40 mA) was used to confirm the ordered framework structure of MOF-5_A (chloroform exchanged) and MOF-5_B crystals (thermally activated). The nitrogen sorption isotherm at 77 K following the thermal activation was measured by an Autosorb-1 (Quantachrome) instrument to evaluate the SSA, the pore size, and the pore volume of the MOF-5_B crystal.

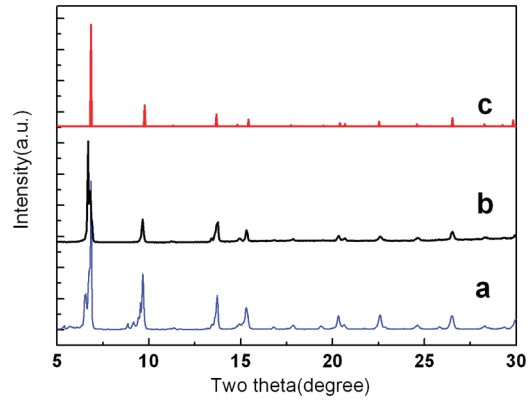

Figure 1. Comparison of powder XRD patterns measured for MOF-5_A (a) and MOF-5_B (b) crystals with that of the calculated pattern (c).[26] The structural coordinates for calculated pattern are listed in Table 1 of ref 26.

Characterization Methods. The SAXS experiments[23] were performed with a Bruker NANOSTAR SAXS instrument. The scattered intensity was collected with a 2D multiwire channel detector. Through the standard data reduction procedure, the collected SAXS intensity data were expressed as a function of the scattering vector Q, where $Q = 4\pi\lambda^{-1} \sin(\vartheta)$, with 2ϑ and λ being the scattering angle and the incident X-ray wavelength, respectively. The pore structure and pore orientation can be directly deduced from 1D SAXS profiles and 2D SAXS patterns, respectively. For investigating the effect of heterogeneous electronic structure due to Zn atoms, the anomalous small-angle X-ray scattering (ASAXS)[24] with two synchrotron X-ray energies (9.6 keV: near K absorption edge of Zn; 10.5 keV: off absorption edge) was conducted. A Hitachi S800 scanning electron microscope (SEM) was employed to observe the morphology of prepared MOF-5 crystals in real space.

In Situ SAXS Measurements. One measurement was performed for MOF-5_A crystal during the heating process to reveal the effect of temperature on the structural evolutions of both mesopores and micropores. The heating process was conducted under vacuum from 25 to 250 °C with an increment of 25 °C. The times for temperature equilibration and data collection were both 30 min at each temperature. After this measurement, the sample was cooled to 200 °C. Another measurement was performed during the subsequent activation at 200 °C to investigate the temporal evolution of structure. The time interval for data collection was 1 h.

Results and Discussion

The XRD patterns of MOF-5_A and MOF-5_B crystals agree well in both peak position and relative intensity with the theoretical pattern calculated from the typical MOF-5 phase (*Fm*3*m* symmetry; lattice constant = 25.5 Å),[25,26] as displayed in Figure 1. The measured nitrogen adsorption−desorption isotherm of MOF-5_B crystal shows the type-I profile (Supporting Information), which is characteristic of micropore filling. The BET SSA and mean pore size determined from the nitrogen isotherm analysis are 4181 m^2/g and 1.7 nm, respectively. The relative pressure (P/P_0) range in the BET analysis is 0.009−0.04 according to the literature[12,13] (Supporting Information). The isotherm curve and XRD pattern demonstrate that the MOF-5_B crystal is highly porous. The measured BET SSA value is somewhat higher than the accessible SSA theoretically calculated from MOF-5 crystallography (3600 m^2/g)[13] due to the error of weighing the relatively light sample (35.6 mg) and the

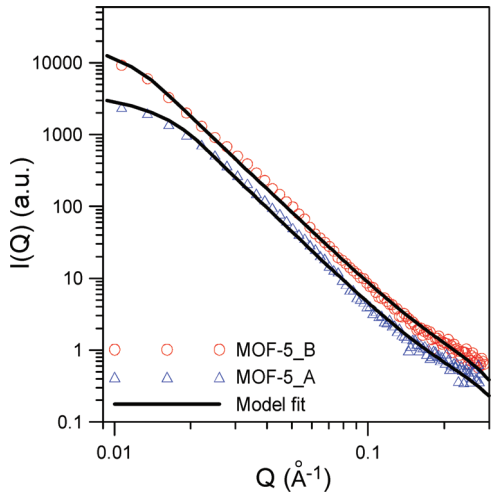

Figure 2. SAXS profiles of MOF-5_A and MOF-5_B samples fitted by eq 1 (solid curves). The low-Q intensities show the characteristic of Guinier approximation of mesopores.

inherent uncertainty of the instrument. The recent BET SSA value of MOF-5 reported by Yaghi's group is 3800 m^2/g.[14] It is believed that the MOF-5_B crystal prepared here has SSA close to the theoretically accessible SSA.[12,13] Consequently, the effect from the local lattice defects previously mentioned was minimized for both MOF-5_A and MOF-5_B crystals. Thus, all structural evolutions observed in the present study were only related to the solvent removal and thermal effect.

Figure 2 displays the SAXS profiles of MOF-5_A and MOF-5_B crystals after the data reduction and background subtraction from high-Q intensity. The observed SAXS patterns are substantially different from those of the MOF-5-like crystals with SSA values less than 1000 m^2/g reported previously. Our previous SAXS model analysis[23] demonstrated that MOF-5 crystals (with BET SSA range of 2800−800 m^2/g) were characterized by (1) the typical porous structure with spherical micropores and mesopores (here, the pore channels between micropores were collapsed into fine channels undetectable under the resolution and Q-range of SAXS) and (2) typical fractal network formed by the aggregation of mesopores. The pore structure evolved due to the increasingly collapsed framework and mesopore aggregation, as was also evidenced by the decrease of SSA values. It was found that the SAXS profiles observed in the present study fail to be fitted by the previously used SAXS models (i.e., sphere, infinite cylinder, and bimodal models). The main reason is that the conventional models are only applicable to the isolated heterogeneities. It seems that these models cannot be applied to the 3D-extended (nearly space filling) pore network consisting of orthogonal nanoscale channels.

It is a big challenge to model the SAXS pattern associated with the pore structure with orthogonal channels. Fortunately, an analytical model[27] developed to describe the fractal networks of nanopores in active carbon (AC) of high SSA and very large volume fraction was found to be able to fit the observed SAXS profiles well via an appropriate modification. The AC with a high SSA was reported to consist of spherical micropores (<2 nm) and a fractal network formed by nanopore channels.[27] The characteristic of fractal is a kind of self-similarity extended from ca. angstrom scale to tens or hundreds of nanometers. The term "nanopore" is not related to any definition of International Union of Pure and Applied Chemistry (IUPAC). Our SAXS result will show that the width of a nanopore channel in the MOF-5 system is found to be in the defined range of micropores (<2 nm). In this case, the SAXS intensity $I(Q)$ scattered from both (1) the fractal network of nanopore channels with the fractal dimension D_P and the channel width L_{ch} and (2) the spherical mesopores with the diameter D_{meso} can be expressed as follows:

$$I(Q) = I_P[1 + (QL_{ch}/2)^{-D_P}] \exp(-Q^2L_{ch}^2/20) + I_0 \exp(-Q^2D_{meso}^2/20) \quad (1)$$

where I_P and I_0 are related to the volume fractions of pore-fractal structure and mesopores, respectively. The scattering intensity calculated from the first term describing the fractal channel network contributes to the scattering in the intermediate- and high-Q region; in particular, a power-law intensity decay is usually manifested in the intermediate-Q region. The exponent associated with the power law is related to the fractal dimension. The expression of the first term is valid for $Q \geq 2\pi/L_{max}$ (i.e., starting from the onset of power-law scattering region), with L_{max} being the network diameter (which prescribes the cutoff of the fractal regime). The exponential expression of the second term is the Guinier approximation for the mesopores, which mainly contributes to the scattering in the low-Q region.

The measured SAXS profiles can be fitted well by using the model of eq 1 (cf. the solid curves in Figure 2). The channel widths of nanopore in the fractal network determined from the fittings for both MOF-5_A and MOF-5_B crystals are 1.2 nm (the error bars are 15−20%). These values are consistent with that obtained by XRD analysis.[28] It is noted that the 3D structure of orthogonal channels in the materials is not strictly fractal. The intersection segments of constituent channels are characteristic of branches and orthogonal order so that they are considered to be fractal-like, as evidenced by the agreement with SAXS model fitting. The determined values of L_{max} for both crystals are 20.9 nm (corresponding to $Q = 0.03$ $Å^{-1}$). Comparing to the AC system with L_{max} of 100−300 nm, this much smaller value explains that the space domain fulfilled with fractal approximation is not large but reasonable. The fractal dimension is determined to be 3.3 by model fitting, which is similar to that of teh AC system and is indicative of very large volume fraction. The excess part of the fractal dimension over 3.0 is an omissible error from the fractal-like approximation. Unlike the AC systems with coexistence of nanochannel and micropores, the present work shows that the geometry of elementary micropores in high-SSA MOF is channel-like rather than sphere-like. In conclusion, the SAXS model with fractal approximation is feasible for interpreting the spatial network consisting of the very large volume fraction of channel network in MOF compared to other models. The mesopore sizes of MOF-5_A and MOF-5_B crystals are determined to be 26.7 and 37.5 nm, respectively. The difference between them is considered to stem from the thermal activation at 200 °C, which will be explained later. It is noted that the model approximation adopted here may not work rigorously for the real pore structure; however, the SAXS analysis demonstrates (at least semiquantitatively) the very large volume fraction of spatial network (at a large scale). It is well-known that numerous independent structure analyses have been performed by both X-ray diffraction[25,28] and neutron diffraction[29] to yield the atomic-scale resolution of the periodic lattice of micropore. Combining both methods can hence yield the structure details from local scale to global scale (showing high microporosity with ordered channels).

During heating from 25 to 250 °C, the pore channel and the constructed network (by the micropores with width <2 nm) remained thermally stable and unchanged in size, as signified

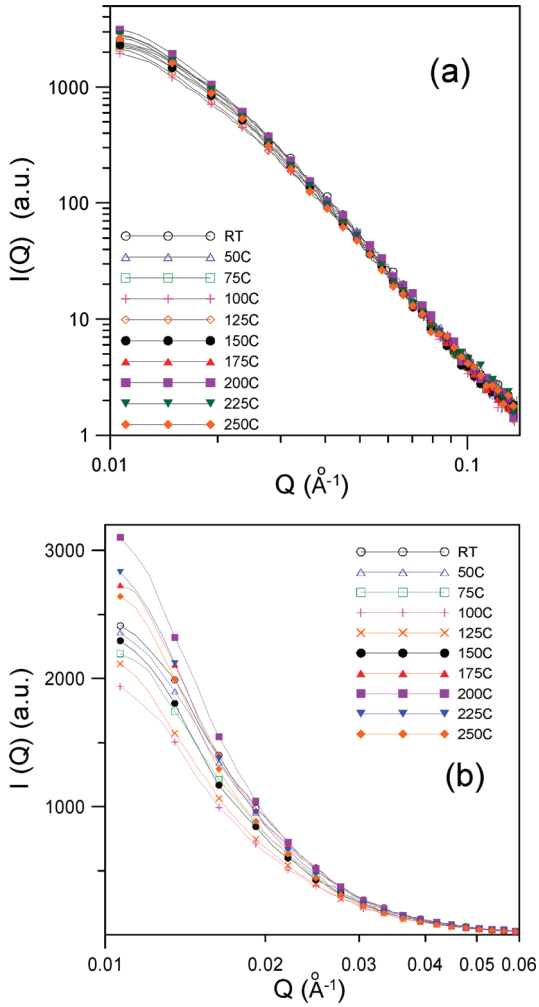

Figure 3. (a) Temperature-dependent SAXS profiles of MOF-5_A crystal during heating from 25 to 250 °C. (b) Temperature-dependent SAXS profiles (linear scale) in the low-Q region, revealing the structural evolution of mesopores.

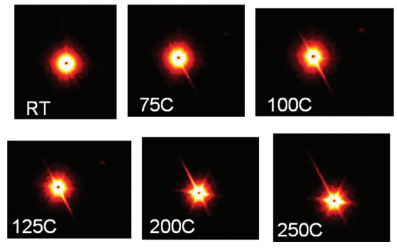

Figure 4. Two-dimension SAXS patterns measured at room temperature, 75, 100, 125, 200, and 250 °C corresponding to Figure 3.

by the unperturbed scattering profiles in the intermediate- and high-Q regions in Figure 3a. On the other hand, the obvious dependence of the SAXS profile in the low-Q region on temperature indicates the occurrence of structural evolution for the mesopores (Figure 3b). The corresponding 2D SAXS patterns (around the low-Q region) are selectively demonstrated in Figure 4 to reveal the spatial orientation of mesopores. Figure 3b shows that the scattering intensity decreases with increasing the temperature from 25 to 100 °C, revealing the shrinkage of mesopores due to the solvent removal. The removal of absorbed water was expected to be complete below 50 °C. A sharp decrease of intensity at 75−100 °C corresponds to the removal of chloroform, signaling a complete exchange of solvent (DEF was replaced by chloroform). At this stage, it was found that the mesopore began to realign toward a preferred orientation (Figure 4). This orientation may coincide with the orientation of micrograins (inside MOF-5 crystal) whose latent boundary was gradually developing. Our SEM observation on the morphologies of selected MOF-5_A and MOF-5_B samples (Figure 5 and Supporting Information) shows a difference in local texture due to the effect of thermal activation (annealing) on the preparation of MOF_B. Figure 5b shows several ditches on the crystalline particles, which are related to the boundary of micrograins with mesopore network along it. The presence of these ditches, however, does not affect the crystal quality as seen from the XRD pattern (Figure 1). It can also be deduced that the space accommodating the mesopores should be located along the micrograin boundary to reduce the surface energy and defects of the polycrystalline system. It can be conjectured that the mesopores are not embedded in the interior of MOF grain because the swelling and shrinkage of mesopores do not destroy the lattice structure of micropores. The SAXS profiles (Figure 3a) show that the micropores during heating remained unchanged. In addition, the PXRD patterns (Figure 1) show the enhancement of crystalline order (or ordered micropore) upon heating. This can be explained as follows. The highly oriented micrograins were formed inside the MOF-5_B crystal based on the morphological observation by SEM (Figure 5b). In the polycrystalline MOF-5_B, the defects and microvoid usually prefer to gather around the boundary of micrograins and continue to grow into large pores to reduce the surface energy of the system, especially in the step of thermal annealing (activation process). This thermodynamic driving force causes the mesopores along the micrograin boundary to begin to migrate and then grow or coalesce. Therefore, the significant shrinkage and reorganization into preferred orientation of mespores occurred concurrently, as evidenced by the 1D and 2D SAXS profiles, respectively.

The SAXS profiles in Figure 2 show that the fraction of mesopores is very small. The zero-angle SAXS intensity (i.e., $I(0)$) is proportional to the product of the volume fraction and the cube of pore radius. The SAXS intensity in the low-Q region is hence able to give a much stronger indication as to the existence of mesopores ($I \propto R^3$) than the gas adsorption method although the mesopore volume fraction is relatively low. In this work, the measured trace of the gas adsorption isotherm cannot accurately reflect the existence of a small amount of mesopores. On the other hand, both the BET analysis and SAXS result show that MOF-5 is highly porous. A combination of these two methods can thus obtain complementary structure information. According to the SAXS data, the shrinkage of mesopores at 250 °C may lead to little reduction of total SSA because the microporous quality is essentially unaffected. It may be concluded that activation (annealing) at 200 °C can effectively maintain the SSA value due to the change of mesopores structure. The scattering profile of the MOF-5_A crystal measured at 200 °C (Figure 3a) is close to that of the MOF-5_B crystal (Figure 2) after the normalization (Supporting Information). This information shows that the temperature effect is more important than the effects of heating rate or time.

The SAXS profiles in Figure 3b further show that the intensity increases with the increasing temperature from 100 to 200 °C, which reveals the swelling of mesopores in this temperature range. This phenomenon is accompanied by the obvious distribution of pore orientation (Figure 4). The reasons are (1) the mesopores have no obstacle to swell after the complete evacuation in pore and (2) the mesopores along the micrograin boundary begin to migrate and then grow or coalesce due to

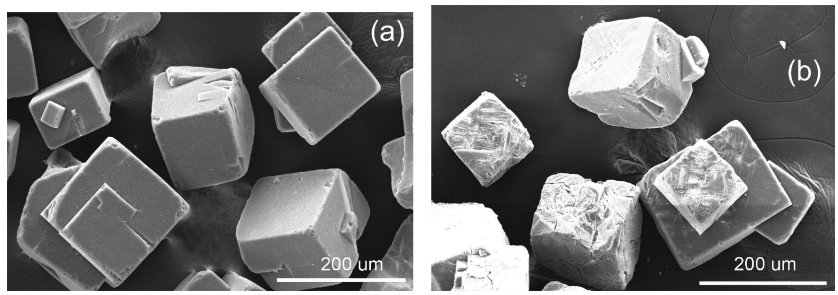

Figure 5. SEM pictures of cubed-shaped MOF-5_A (a) and MOF-5_B (b) crystals.

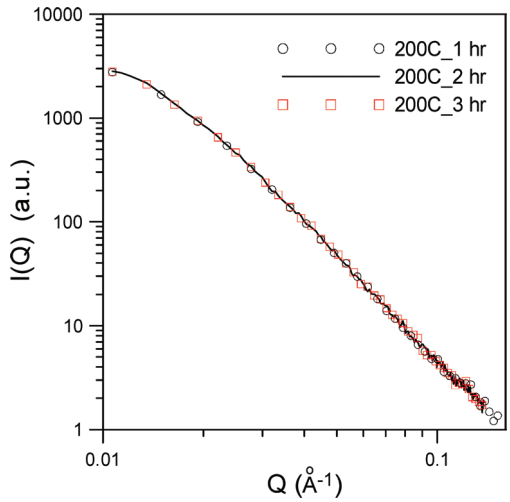

Figure 6. Time-resolved SAXS profiles of MOF-5_A crystal during thermal activation at 200 °C.

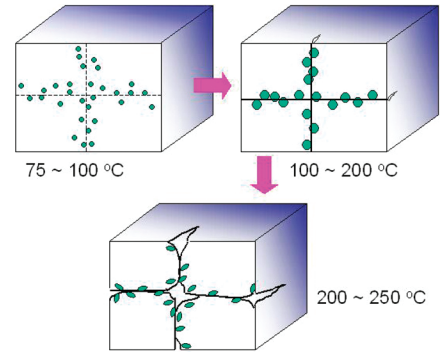

Figure 7. Schematic illustration of the structural evolution and spatial distribution of the mesopores formed concurrently with micrograin boundary.

the thermal annealing effect. Meanwhile, the ordered arrangement of mesopores along the developing boundary takes place. The resulting mesopores at 200 °C are larger than the original pores at room temperature, giving a reasonable explanation to the difference in SAXS intensity observed in Figure 2. More interestingly, the SAXS profiles in Figure 3b demonstrate that the mesopores shrink again with increasing temperature from 200 to 250 °C. We conjectured that the micrograin boundaries squeeze each other due to the increase of crystalline ordering, leading to a compression of the mesopores on the boundary. In conclusion, the mesopores concentrated at the micrograin boundary are indeed flexible, which can be tuned by the temperature. This finding is only for high-SSA MOF-5 and has never been reported before. In the subsequent activation at 200 °C for 3 h, the SAXS profiles (Figure 6) do not vary with the time, showing that the structure has reached stable state. In contrast to the insensitive effect of heating time on the pore structure, temperature is the key parameter for shrinkage, swelling, and alignment of the mesopores.

The SAXS result, discussed in the last two paragraphs, is summarized as a schematic illustration in Figure 7 for the structural evolution and spatial distribution of the mesopores formed concurrently with micrograin boundary. Main steps during heating are (1) mesopores' shrinkage and realignment along the micrograin whose latent boundary begins to form and gradually propagate (75−100 °C), (2) the growth or coalescence of mesopores along the increasingly developing boundary (100−200 °C), and (3) shrinkage of mesopores due to the slight alignment of the well-formed boundary (200−250 °C). An important deduction about the material characteristic and performance is addressed as follows. The network connected by mesopores on the micrograin boundaries provides a necessary path for gas molecules to thoroughly migrate to the interior of the crystal and also serves as a main entrance into the micrograin from boundary surface. In practice, the new obstacles or defects will easily form at the interface due to the packing, handing operation, and sample decomposition. They will affect the gas diffusion along nanopore channel into the interior. For the usual MOF-5 crystals with lattice defects (partly collapsed framework) as the diffusion hindrance for gas molecule, the mesopore network is a key path helping molecules bypass the lattice defects and reducing the blockage effect. To date, it is difficult to distinguish between the practical roles of mesopore and micropore networks transporting the gas molecules. It appears that mesopore and micrpore networks are similar to the vein and blood capillary, respectively, in the human body. Thus, controlling the mesopores and their network along the orientation direction of the micrograins by certain routes is an effective way to increase SSA value measured by nitrogen molecules and thus the adsorption for the potential applications. The mesopores and micropores during the subsequent cooling remain unchanged, also indicated by the SAXS observation. The mesopores (or void defects) along the micrograins seem to be flexible and swell during the subsequent room temperature storage due to the unknown factors (e.g., sample decomposition or humidity etc.). Thus, the heating effect in the next thermal cycle can result in a slight shrinkage of mesopores.

It is interesting and important to understand the limitation or drawbacks of applying SAXS technique to characterize MOF and then make an appropriate correction. Note that a significant difference between the typical microporous materials and MOF is the $Zn_4O(CO_2)_6$ clusters distributing at four corners around the spherical pseudomicropore (i.e., MOF-5 lattice cell), leading to local nonuniformity of electronic density structure of micropore. SAXS probes the structure of material through the interaction of X-ray with electrons, whereas another technique, small-angle neutron scattering (SANS), involves the interaction of neutron with atomic nuclei. A study about microporous

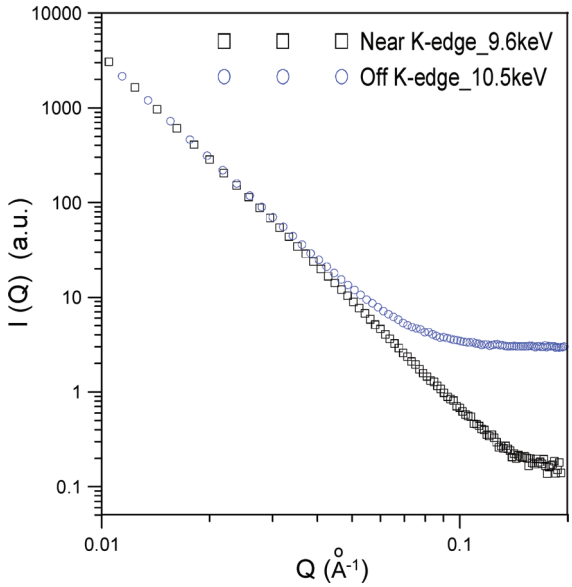

Figure 8. A comparison of anomalous synchrotron SAXS profiles with near K-edge absorption energy (9.6 keV) with that obtained from the off-absorption energies (10.5 keV) of Zn for a MOF-5 with an SSA value of ~1000 m^2/g.

carbons demonstrated that there was a difference between SAXS and SANS profiles in the high-Q region (corresponding to micropore size range) due to the electronic structure within the micropores.[17] It was suggested that combining SAXS and SANS can make a reliable justification of the real pore structure because SAXS mainly provides the information of electronic density structure of micropores rather than atomic structure. The present study uses the anomalous synchrotron SAXS with near K-edge absorption energy of Zn atom instead of SANS to yield the condition of a uniform electronic structure (like the atomic contrast) seen by X-ray. Figure 8 shows the anomalous synchrotron SAXS profiles for the MOF-5 crystal (SSA value: ~1200 m^2/g) as an example. The characterization of this crystal has been reported previously.[23] The result is consistent with that of the previous study combining SAXS and SANS. The SAXS profile obtained using the off-absorption energy shows the higher intensities in the high-Q region than that using the near K-edge absorption energy of Zn. This can be ascribed to (1) the local variation in electronic density due to Zn atoms within the micropores and (2) the background contributed by the first diffraction peak (i.e., 6.9° peak) enhanced by ordered Zn atoms. We found that the latter dominates by examining the simultaneous anomalous wide-angle X-ray scattering (WAXS) and SAXS data. The present study concluded that the deviation in the SAXS data from Zn atoms could be eliminated through the careful subtraction considering the contribution of high-Q intensity obtained from the simultaneous WAXS or diffraction.

Conclusion

For the high-SSA MOF-5 crystal, SAXS analysis was capable of providing a complete characterization of the pore structure. The present study has adopted a model that uniquely described the spatial networks consisting of both pore channels (1.2 nm in width) and mesopores (30−40 nm in size) in the high-SSA MOF. The pore channels (micropores) are not affected by the heating from 25 to 250 °C. The anomalous synchrotron SAXS/WAXS was conducted to evaluate the effect of electronic structure and establish the right approach of data reduction. Combination of in situ 1D and 2D SAXS patterns revealed the concurrent evolution (shrinkage, swelling, and orientation) of mesopore structure and micrograin boundary during different thermal treatments. The activation at 200 °C can optimally maintain the SSA value due to the change of mesopore structure. According to our experimental observations, the network connected by mesopores along the concurrently developing micrograin boundary can be tuned by temperature. The mesopore network is a necessary path for gas molecules to thoroughly migrate to the interior of the crystal and serves as a main entrance into the micrograins from the boundary surface. Consistently, the study of Hupp's group using supercritical solvent[22] preliminarily points out that the inhibition of mesopore collapse substantially increases the accessible SSA (or micropore accessibility). The understanding and control of mesopore structure will provide new routes for improving the general MOF systems for potential applications.

Acknowledgment. We thank Dr. Huan-Hsiung Tseng for the assistance with the SEM experiment and Prof. Sow-Hsin Chen (Massachusetts Institute of Technology) for academic support.

Supporting Information Available: Nitrogen sorption analyses at 77 K for MOF-5_B crystal and MOF5_A crystals activated at different temperatures, SEM pictures for MOF-5_A and MOF-5_B crystals, and the normalization of SAXS profiles. This material is available free of charge via the Internet at http://pubs.acs.org.

References and Notes

(1) Rowsell, J. L. C.; Eckert, J.; Yaghi, O. M. *J. Am. Chem. Soc.* **2005**, *127*, 14904–14910.
(2) Pan, L.; Sander, M. B.; Huang, X.; Li, J.; Smith, M.; Bittner, E.; Bockrath, B.; Johnson, J. K. *J. Am. Chem. Soc.* **2004**, *126*, 1308–1309.
(3) Rowsell, J. L. C.; Millward, A. R.; Park, K. S.; Yaghi, O. M. *J. Am. Chem. Soc.* **2004**, *126*, 5666–5667.
(4) Wong-Foy, A. G.; Matzger, A. J.; Yaghi, O. M. *J. Am. Chem. Soc.* **2006**, *128*, 3494–3495.
(5) Li, Y.; Yang, F. H.; Yang, R. T. *J. Phys. Chem. C* **2007**, *111*, 3405–3411.
(6) Miller, M. A.; Wang, C. Y.; Merrill, G. N. *J. Phys. Chem. C* **2009**, *113*, 3222–3231.
(7) Bastin, L.; Barcia, P. S.; Hurtado, E. J.; Silva, J. A. C.; Rodrigues, A. E.; Chen, B. J. *J. Phys. Chem. C* **2008**, *112*, 1575–1581.
(8) Wu, C. D.; Hu, A.; Zhang, L.; Lin, W. *J. Am. Chem. Soc.* **2005**, *127*, 8940–8941.
(9) Panella, B.; Hirscher, M. *Adv. Mater.* **2005**, *17*, 538–541.
(10) Huang, L.; Wang, H.; Chen, J.; Wang, Z.; Sun, J.; Zhao, D.; Yan, Y. *Microporous Mesoporous Mater.* **2003**, *58*, 105–114.
(11) Hafizovic, J.; Bjϕrgen, M.; Olsbye, U.; Dietzel, P. D. C.; Bordiga, S.; Prestipino, C.; Lamberti, C.; Lillerud, K. P. *J. Am. Chem. Soc.* **2007**, *129*, 3612–3620.
(12) Walton, K. S.; Snurr, R. Q. *J. Am. Chem. Soc.* **2007**, *129*, 8552–8556.
(13) Düren, T.; Millange, F.; Férey, G.; Walton, K. S.; Snurr, R. Q. *J. Phys. Chem. C* **2007**, *111*, 15350–15356.
(14) Kaye, S. S.; Dailly, A.; Yaghi, O. M.; Long, J. R. *J. Am. Chem. Soc.* **2007**, *129*, 14176–14177.
(15) Castillo, J. M.; Vlugt, T. J. H.; Calero, S. *J. Phys. Chem. C* **2008**, *112*, 15934–15939.
(16) Greathouse, J. A.; Allendorf, M. D. *J. Am. Chem. Soc.* **2006**, *128*, 10678–10679.
(17) Hall, P. J.; Brown, S.; Fernandez, J.; Calo, J. M. *Carbon* **2000**, *38*, 1257–1259.
(18) Bock, V.; Emmerling, A.; Saliger, R.; Fricke, J. *J. Porous Mater.* **1997**, *4*, 287–294.
(19) Gille, W.; Enke, D.; Janowski, F. *J. Phys. Chem. Solids* **2003**, *64*, 2209–2218.
(20) Smarsly, B.; Göltner, C.; Antonietti, M.; Ruland, W.; Hoinkis, E. *J. Phys. Chem. B* **2001**, *105*, 831–840.
(21) Kepert, C. J.; Rosseinsky, M. J. *Chem. Commun.* **1999**, (4), 375–376.
(22) Nelson, A. P.; Farha, O. K.; Mulfort, K. L.; Hupp, J. T. *J. Am. Chem. Soc.* **2009**, *131*, 458–460.

(23) Tsao, C. S.; Yu, M. S.; Chung, T. Y.; Wu, H. C.; Wang, C. Y.; Chang, K. S.; Chen, H. L. *J. Am. Chem. Soc.* **2007**, *129*, 15997–16004.

(24) Tsao, C. S.; Yu, M. S.; Wang, C. Y.; Liao, P. Y.; Chen, H. L.; Jeng, U. S.; Tzeng, Y. R.; Chung, T. Y.; Wu, H. C. *J. Am. Chem. Soc.* **2009**, *131*, 1404–1406.

(25) Li, H.; Eddaoudi, M.; O'Keeffe, M.; Yaghi, O. M. *Nature* **1999**, *402*, 276–279.

(26) Mulder, F. M.; Dingemans, T. J.; Wagemaker, M.; Kearley, G. *J. Chem. Phys.* **2005**, *317*, 113–118.

(27) Pfeifer, P.; Ehrburger-Dolle, F.; Rieker, T. P.; Gonzalez, M. T.; Hoffman, W. P.; Molina-Sabio, M.; Rodriguez-Reinoso, F. P.; Schmidt, W.; Voss, D. *Phys. Rev. Lett.* **2002**, *88*, 115502-1–115502-4.

(28) Rowsell, J. L. C.; Spencer, E. C.; Eckert, J.; Howard, J. A. K.; Yaghi, O. M. *Science* **2005**, *309*, 1350–1354.

(29) Yildirim, T.; Hartman, M. R. *Phys. Rev. Lett.* **2005**, *95*, 215504-1–215504-4.

JP907103R